

Multimode ambient noise double-beamforming tomography with a dense linear array: revealing accretionary wedge architecture across Central Taiwan

Cheng-Nan Liu¹,^{ORCID} Fan-Chi Lin,¹ Hsin-Hua Huang,^{2,3} Yu Wang³ and Konstantinos Gkogkas^{1,4}

¹*Department of Geology and Geophysics, University of Utah, Salt Lake City, UT 84112, USA. E-mail: Cheng-Nan.Liu@utah.edu*

²*Institute of Earth Sciences, Academia Sinica, Taipei 11529, Taiwan*

³*Department of Geosciences, National Taiwan University, Taipei 10617, Taiwan*

⁴*Department of Lithospheric Research, Institute of Geophysics, Polish Academy of Science, 01-452 Warszawa, Republic of Poland*

Accepted 2024 August 7. Received 2024 July 2; in original form 2024 January 28

SUMMARY

Taiwan, one of the most active orogenic belts in the world, undergoes orogenic processes that can be elucidated by the doubly vergent wedge model, explaining the extensive island-wide geological deformation. To provide a clearer depiction of its cross-island orogenic architecture, we apply ambient noise tomography across an east–west linear seismic array in central Taiwan, constructing the first high-resolution 2-D shear velocity model of the upper crust in the region. We observe robust fundamental- and higher-mode Rayleigh waves, with the latter being mainly present in the western Coastal Plain. We develop a multimode double-beamforming method to determine local phase velocities across the array between 2- and 5-s periods. For each location, we jointly invert all available fundamental- and higher-mode phase velocities using a Bayesian-based inversion method to obtain a 1-D model. All 1-D models are then combined to form a final 2-D model from the surface to ~10 km depth. Our newly developed 2-D model clearly delineates major structural boundaries and fault geometries across central Taiwan, thereby corroborating the previously proposed pro-wedge and retro-wedge models while offering insight into regional seismic hazards.

Key words: Crustal imaging; Seismic interferometry; Seismic noise; Seismic tomography; Surface waves and free oscillations; Crustal structure.

1 INTRODUCTION

The vigorous orogenic activity in Taiwan is attributed to the oblique convergence between the Eurasian Plate (EP) and Philippine Sea Plate (PSP, Suppe 1984; Teng 1990). This oblique convergence causes intense crustal deformation and mountain building, leading to complex geological structure and multiple tectonic units such as the Coastal Plain, Western Foothill, Hsuehshan Range (HSR), Central Range, Longitudinal Valley and Coastal Range from west to east (Fig. 1). As best depicted by the classic thin-skinned tectonic model, the western part of Taiwan is an accretionary wedge formed by a series of folds and thrusts upon a gentle east-dipping decollement (Suppe 1981; Carena *et al.* 2002; Yue *et al.* 2005). In contrast, the eastern part of Taiwan accretionary wedge, primarily encompassing the Central Range, undergoes rapid uplift and exhumation. This could involve severe mid-to-lower-crustal thickening through lithospheric collision (Tsai 1986; Yen *et al.* 1998; Yu & Chen 1994) or underplating (Simoes *et al.* 2007; Chen *et al.* 2022). In a context of the doubly vergent orogenic wedge model (Willett *et al.* 1993; Chuang

et al. 2014), the eastern Central Range acts as the retro-wedge in the orogeny system. The eastern boundary of the retro-wedge is named the Central Range Fault (CRF, Biq 1965; Shyu *et al.* 2006), which plays an important role in mountain building of the Central Range to the west and the formation of the Longitudinal Valley to the east. Based on seismological observations, geodetic measurements and geomorphological mapping, the CRF is suggested to be an active west-dipping reverse and left-lateral fault (Shyu *et al.* 2006; Wu *et al.* 2006; Chuang *et al.* 2014; Huang & Wang 2022), especially after the 2022 September 18 M_w 7.0 Chihshang earthquake in the southern Longitudinal Valley (Lee *et al.* 2023; Tang *et al.* 2023; Lin *et al.* 2024).

The interaction between the EP and PSP has led to complicated structural settings and fault systems in Taiwan, which results in the frequent occurrence of moderate-to-large earthquakes (e.g. Chen *et al.* 2001b; Yue *et al.* 2005; Wu *et al.* 2006; Kuochen *et al.* 2007; Lee *et al.* 2014; Huang & Wang 2022). To further investigate the mechanism/evolution of Taiwan's orogenic belt and active fault behaviours, geophysical and geological studies have been conducted

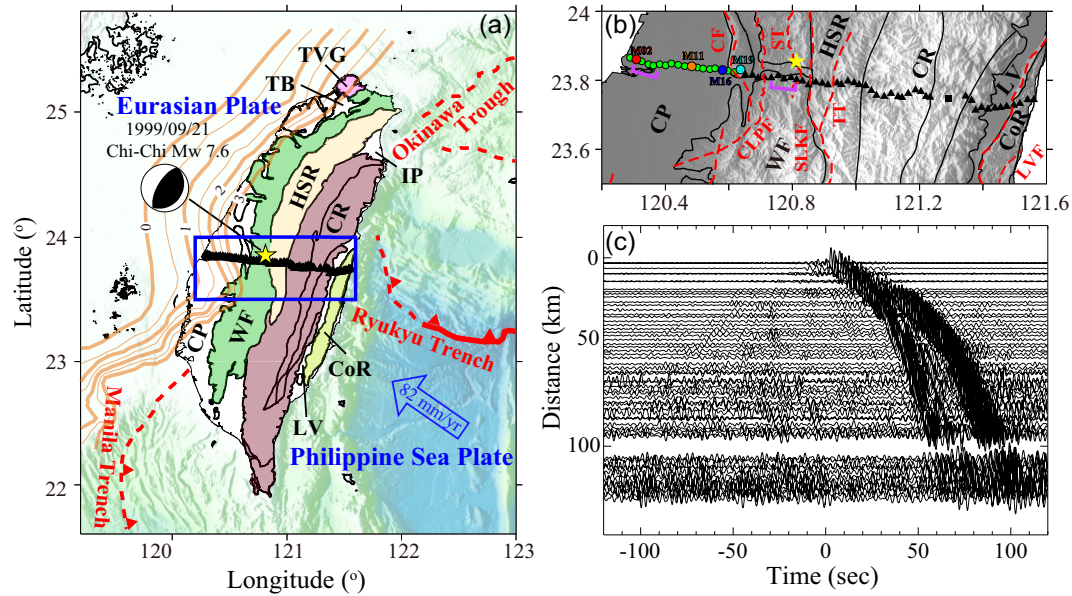


Figure 1. (a) The tectonic map of Taiwan and geophone stations used in this study (black triangles). CP: Coastal Plain. WF: Western Foothills. HSR: Hsuehsan Range. CR: Central Range. LV: Longitudinal Valley. CoR: Coastal Range. TVG: Tatun Volcano Group. TB: Taipei Basin. IP: Ilan Plain. The star represents the epicentre of the 1999 September 21, M_w 7.6 Chi-Chi earthquake where the beach ball represents the focal mechanism (Wu *et al.* 2008). The brown lines correspond to the foreland basin depth contours, adapted from Lin & Watts (2002). The area within the rectangle is shown in (b). (b) The targeted area in this study. Faults and structural boundaries are marked in red dashed and black solid lines, respectively. CF: Changhua Fault. CLPF: Chelungpu Fault. ST: Shuangtung Thrust. SLKF: Shuilikeng Fault. TT: Tili Thrust. LVF: Longitudinal Valley Fault system. The circles mark stations with strong higher-mode signals and brackets show the example source–receiver beam pair used in Fig. 2. The red, orange, blue and cyan circles identify stations M02, M11, M16 and M19 used in later figures. (c) Example 2- to 5-s ZZ CCFs between source station M02 and all other receivers.

including balanced cross-sections (Suppe 1981; Yue *et al.* 2005), local geological and geomorphological mapping (Johnson *et al.* 2001; Shih & Teng 2001; Lee *et al.* 2002), geodetic measurements (Chen *et al.* 2001a; Hsu *et al.* 2007; Ching *et al.* 2011), seismic reflection/refraction imaging (Lai & Chern 2002; Wang *et al.* 2002; Van Avendonk *et al.* 2014, 2016; Kuo *et al.* 2016), geophysical data set analysis (Chang *et al.* 2000; Kao & Chen 2000), earthquake sequences (Chuang *et al.* 2014; Huang & Wang 2022), geological trenching/logging (Wu *et al.* 2007; Hung *et al.* 2009) and seismic tomography (Kuo-Chen *et al.* 2012; Huang *et al.* 2014a, b, 2015). However, limited depth and lateral resolution of existing regional tomography models prevents robust constraints on the geometry of major faults and structural boundaries. Therefore, constraining detailed subsurface fault geometry remains a major challenge despite its importance to the earthquake hazard assessment.

To better understand the upper crustal structure and orogenic evolution, we apply ambient noise tomography (Shapiro *et al.* 2005) across an east–west dense linear geophone array in central Taiwan. The array was deployed as part of the TAIGER (Taiwan Integrated Geodynamic Research) project (Fig. 1; Kuo-Chen *et al.* 2012). Contrary to earthquake-based tomography (e.g. Huang *et al.* 2014a), ambient noise tomography combined with dense seismic arrays has demonstrated superior resolution on illuminating detailed fault and basin structures at shallow depths (Lin *et al.* 2013; Wang *et al.* 2019a; Jia & Clayton 2021; Liu *et al.* 2021; Rabade *et al.* 2023). In this study, we first show that robust fundamental- and higher-mode Rayleigh waves can be observed in the noise cross-correlations across the entire central Taiwan linear array and in the western Coastal Plain, respectively. Second, we describe a modified double-beamforming method (Wang *et al.* 2019a, b; Gkogkas *et al.* 2021) to resolve multimode Rayleigh wave phase velocities. We then invert Rayleigh wave phase velocity measurements to construct a detailed

2-D shear velocity model across central Taiwan. By comparing the 2-D shear velocity model with the regional seismicity, the new model illuminates subsurface structural geometry and supports the doubly vergent wedge model in Taiwan. The model validates (1) the geometry of the Taiwan Main Detachment beneath pro-wedge in western Taiwan and (2) the existence of the CRF, which intersects with the Longitudinal Valley Fault (LVF) systems and contributes to the uplift of the retro-wedge orogen in eastern Taiwan. The new 2-D shear velocity model also provides new insight into the composition and geometry of major geological structures across the orogen.

2 DATA AND METHODS

2.1 Data pre-processing and ambient noise cross-correlation

We use 73 days of continuous waveform data from 2009 March 20 to May 31, recorded by the linear array of the TAIGER project in central Taiwan (Fig. 1; Okaya *et al.* 2009; Kuo-Chen *et al.* 2012). The linear array comprises 56 three-component Mark Products L22 short-period geophones with 2 Hz natural frequency cutting across central Taiwan with station spacing of ~ 2 km (Figs 1a and b). We closely follow the data-preprocessing workflow of Liu *et al.* (2021) on all continuous daily waveforms and construct the multicomponent cross-correlation functions (CCFs). First, we remove instrumental responses, mean and trend from the daily waveforms (Bensen *et al.* 2007) and decimate the sampling rate to 5 Hz. Then, to preserve the relative amplitude between each component, we filter three-component waveforms between 15- and 50-s periods calculate the absolute mean with a 128-s running time window to obtain temporal normalization functions, and then divide the three-component

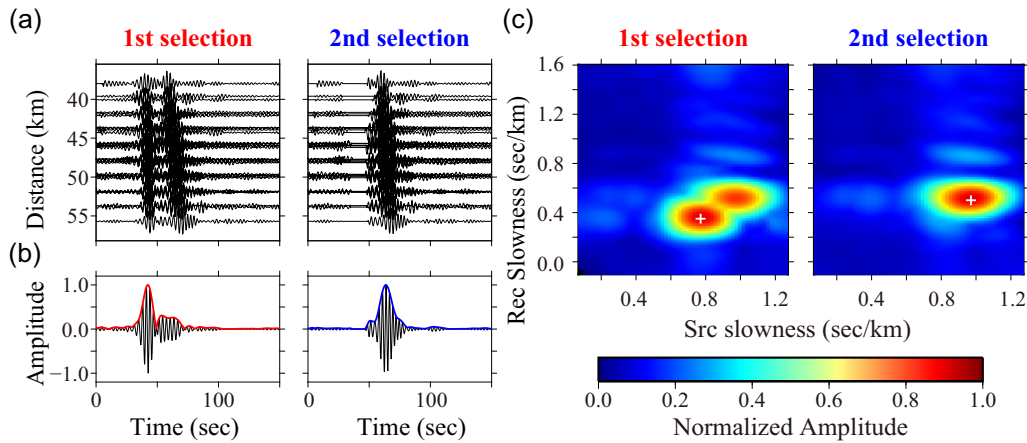


Figure 2. The double-beamforming result of an example source–receiver beam pair (denoted in Fig. 1b). (a) The shifted CCFs in the first and second iterations based on the optimal source and receiver slowness determined in (c). (b) The stacked CCF of the shifted CCFs shown in (a). (c) The beam power determined by source and receiver slowness grid search in the first and second iterations. The white cross identifies the optimal source and receiver slowness values.

unfiltered waveforms by the maximum of three-component temporal normalization functions to suppress the undesired energetic earthquake signals (Lin *et al.* 2014). While 2 Hz geophones are not extremely sensitive to signals above 1-s period, teleseismic signals excited by large earthquakes can still be effectively identified with the 15–50 s bandpass filter (Wang *et al.* 2019b). Next, to whiten the spectrums, we divide the spectrum of each component by the averaged smoothed spectrum of the three-component waveforms. After cross-correlating all the pre-processed daily noise waveforms, we stack and rotate them to obtain nine-component CCFs. In this study, we focus on extracting Rayleigh waves using the vertical–vertical (ZZ) CCFs. In addition, we use the vertical–radial (ZR) component to check the particle motion and exclude non-Rayleigh wave signals. Given that phase velocity measurements exhibit lower uncertainties and possess a deeper sensitivity kernel, revealing deeper structures at the same period compared to group velocity (Lin *et al.* 2008), this study emphasizes the extraction of phase velocity measurements to construct the first isotropic V_s model across central Taiwan. An example of 2–5 s bandpassed ZZ CCF record section is shown in Fig. 1(c), where both fundamental-mode Rayleigh wave and higher-mode/body wave signals can be clearly observed with waves predominantly propagating eastward (Fig. 1c). In this study, for simplicity, we stack the causal and acausal parts of CCFs to construct symmetrical CCFs for following analyses.

2.2 Iterative double-beamforming tomography

Here, we briefly describe the double-beamforming method developed by Wang *et al.* (2019b) and only focus on the modification we made to measure both higher- and fundamental-mode Rayleigh wave phase velocities.

We consider all station locations as possible beam centres for both the source and receiver beams. We fix the beam width as 6 km for all the beams to include sufficient stations (> 4), except for one specific beam centred in the East Central Range (black square in Fig. 1b) where a 20 km beam is used due to the station gap. We only keep source–receiver beam pairs with beam centre distance ≥ 3 wavelengths, assuming a reference velocity of 3 km s^{-1} , to satisfy the far-field approximation (Yao *et al.* 2006). For each source-and-receiver beam pair and each central period, we normalize all available bandpassed CCFs by their maximum amplitudes. We then shift and stack the normalized CCFs, where the time-shift

of each CCF is calculated based on the distances between the source and receiver stations to the source and receiver beam centres, respectively, and the assumed source and receiver phase slowness (i.e. inverse of phase velocity). We perform this shift and stack process in the frequency domain, where a time-shift is equivalent to a phase shift, to avoid the finite time-step limitation. We then transform the stacked waveform back to time domain and consider the maximum waveform amplitude as the beam power. We perform a grid search over both source and receiver phase slowness with the slowness ranging between 0.25 and 2 s km^{-1} .

For single-mode process, the double-beam method described by Wang *et al.* (2019b) would simply take the source and receiver slowness values corresponding to the highest beam power. Here, to account for the multiple energy packages observed (Fig. 1c), we develop an iterative process to separate the fundamental- and higher-mode signals (Fig. 2). In the initial iteration, through grid search, we first determine the source and receiver slowness and the associate group arrival time (t_{max}) that gives the maximum beam power. This corresponds to the primary energy package. We then cut this most energetic phase out from the shifted but unstacked CCFs with a $t_{\text{max}} \pm 0.15T$ signal window where T represents period. Here, we use the instantaneous period of the stacked CCF based on the phase derivative at t_{max} , which deviates slightly from the centre period of the Gaussian bandpass filter used (Lin *et al.* 2008). The cut CCFs are then shifted and stacked again in the follow-up iteration to obtain the phase slowness associated with the secondary energy maximum. By comparing the slowness and the t_{max} from the two iterations, we distinguish potential higher- and fundamental-mode energy based on (1) the higher mode should have lower slowness (higher velocity) and (2) the t_{max} of the higher mode should be smaller than the fundamental mode.

We only keep measurements with the stacked CCF signal-to-noise ratio (SNR) above 8, where the SNR is defined as the ratio between the maximum amplitude within the signal window (determined by 0.5 km s^{-1} minimum and 4.0 km s^{-1} maximum velocities) and the root-mean-square amplitude of the trailing noise. Furthermore, according to the previous study (Tokimatsu *et al.* 1992), the fundamental- and higher-mode Rayleigh waves are expected to have a retrograde and prograde particle motion, respectively. Therefore, we implement a selection criterion based on the ellipticity of the particle motion, where only source-and-receiver pairs with a $75^\circ - 105^\circ$ phase shift between shift and stacked ZZ and

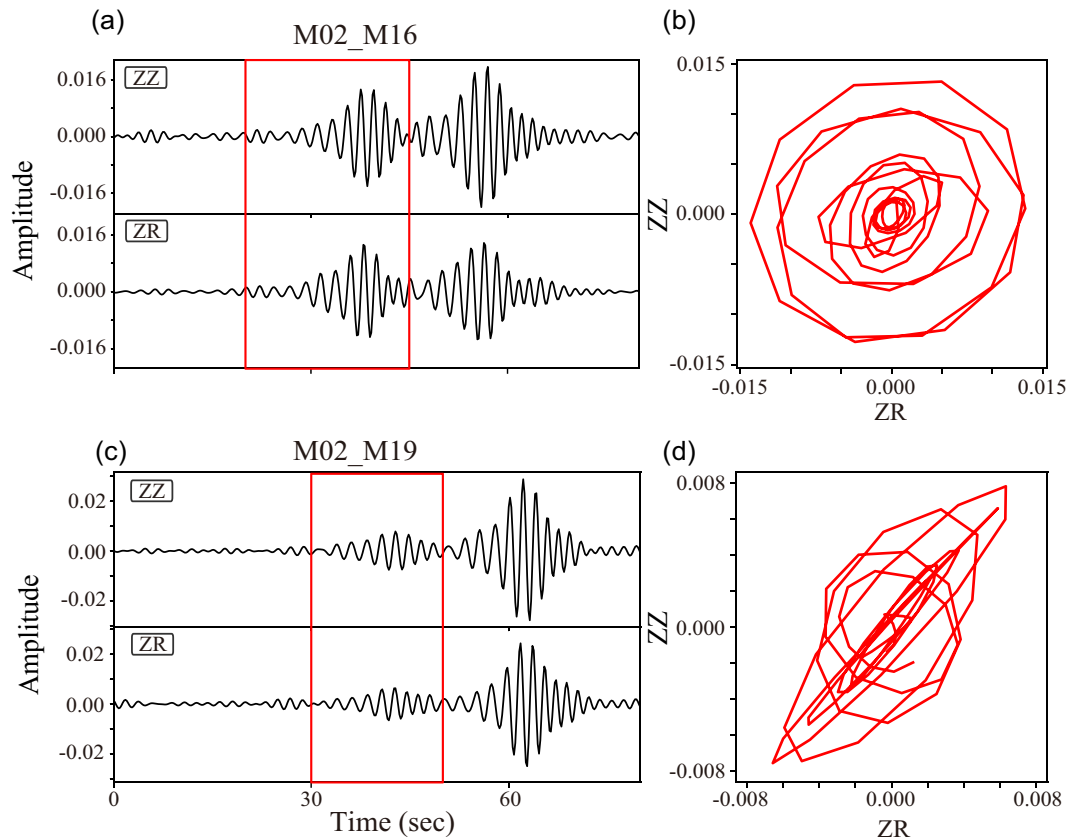


Figure 3. The particle motions for potential higher-mode signals. (a) The ZZ- and ZR-component CCFs with source station M02 and receiver station M16 (red and blue circle in Fig. 1b, respectively). The box indicates the higher-mode time window used in (b). (b) The observed higher-mode elliptical particle motion with a near 90° phase shift between the vertical and horizontal components. (c) and (d) Same as (a) and (b), but for source station M02 and receiver station M19 (red and cyan circle in Fig. 1b, respectively). Note the tilting/linear particle motion which suggests the phase contains scattered body wave energy.

ZR waveforms are kept (Fig. 3). While we observed two energetic phases in most CCFs (Fig. 1c), only stations in the Coastal Plain (green circles in Fig. 1b) show robust higher-mode prograde particle motion. This is consistent with previous studies that observed higher-mode Rayleigh waves in thick sedimentary settings (Tanimoto & Rivera 2005; Savage *et al.* 2013; Jiang & Denolle 2022). In contrast, stations east of Coastal Plain show linear/tilting instead of prograde/retrograde particle motions, suggesting that the higher-mode energy likely scattered and converted into body waves when entering the mountain terrain (Figs 3c and d). Studying mode conversion is outside of the scope of this study and will be the subject of future investigation.

For each period, beam centre location, and each mode, we estimate the phase velocity and its uncertainty based on the mean and the standard deviation (STD) of the mean of all available measurements (Figs 4b and c). All measurements outside of 2.5 STD are considered outliers and removed from the final statistics. To be conservative and account for unaccounted wave phenomena such as finite-frequency effect, off-great-circle propagation and effect of topography variation, all uncertainties were scaled up empirically by a factor of 1.5 for later Markov Chain Monte Carlo (MCMC) inversion. To highlight the kinks in the observed fundamental-mode phase velocity profiles, for each station location, we calculate the absolute spatial second derivative of phase velocity using the nearest stations on each side (Figs 4e and f). While not exactly one to one, many of the locations with elevated second derivative values coincide with the mapped fault locations and structural boundaries, particularly at the 4-s period.

2.3 Markov Chain Monte Carlo joint inversion

In this study, we follow an MCMC Bayesian inversion method (Shen *et al.* 2013) to invert available higher- and fundamental-mode dispersion measurements jointly. For each beam centre location, we describe the 1-D V_s velocity model down to a depth of 15 km using six cubic B-splines underlain by a half space model. The V_p and density are set using the empirical relationship described by Brocher (2005). At each location, we extract a 1-D reference model from the 3-D regional model of Huang *et al.* (2014a) to use as the starting model for the inversion. To stabilize the inversion, in addition to the short-period (2–5 s) dispersion measurements from this study (Fig. 5a), we include 10 to 12-s fundamental-mode Rayleigh wave phase velocities forward calculated using the 1-D reference model. We impose a 10 per cent uncertainty for those ad hoc 10 to 12-s phase velocities, which is larger than the ~ 3 per cent uncertainty for the measurements made in this study.

For each location, we randomly perturb the 1-D model (3000 iterations, 16 jumps, up to 75 per cent variation relative to the starting model parameters) and forward-calculate Rayleigh wave dispersion curves (Herrmann 2013). We reject unrealistic models with V_s above 4.9 km s^{-1} and only accept posterior models with χ^2 misfits within ± 0.5 of the minimum misfit model. We do not impose any additional weighting between the fundamental- and higher-mode measurements beyond the estimated uncertainties. We then derive the final 1-D V_s model and its uncertainty based on the mean and the STD of the mean of all acceptable models (Figs 7a–c). The predicted phase velocities forward calculated using the inverted model are overall consistent with the measured phase velocities

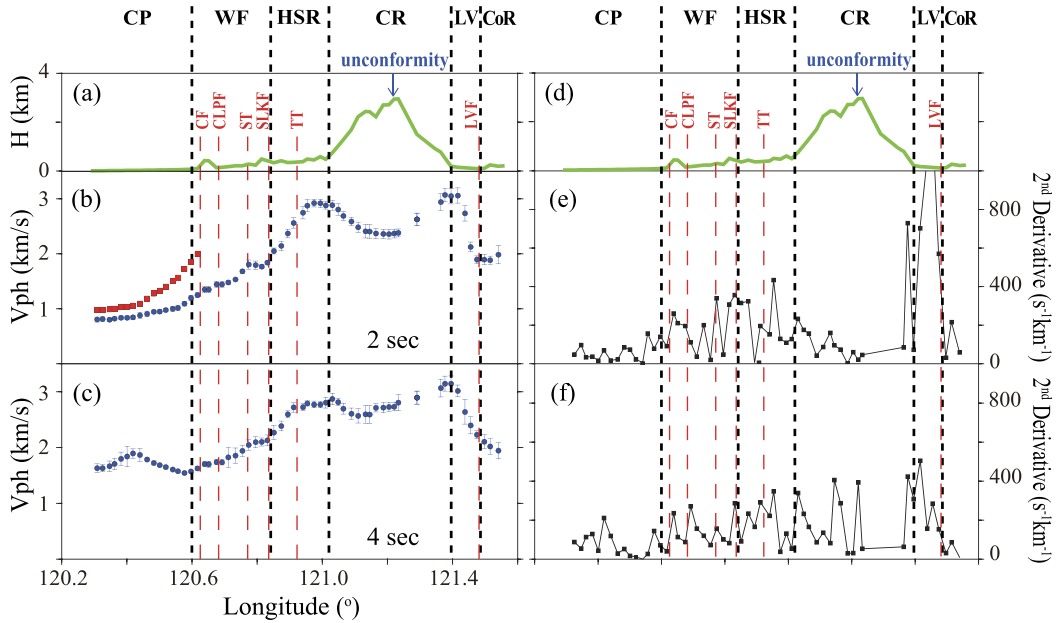


Figure 4. (a) and (d) The elevation across the seismic array. The red dashed and black dotted lines denote faults and structural boundaries from Yue *et al.* (2005). (b) The 2-s phase velocity profile derived using double beamforming. The red triangles and blue dots with error bars correspond to higher- and fundamental-mode phase velocities, respectively. (c) Same as (b), but for 4 s. Only fundamental-mode signals are observed at 4 s. (e) The 2-s absolute second derivative profile of fundamental-mode phase velocity. (f) Same as (e), but for 4 s.

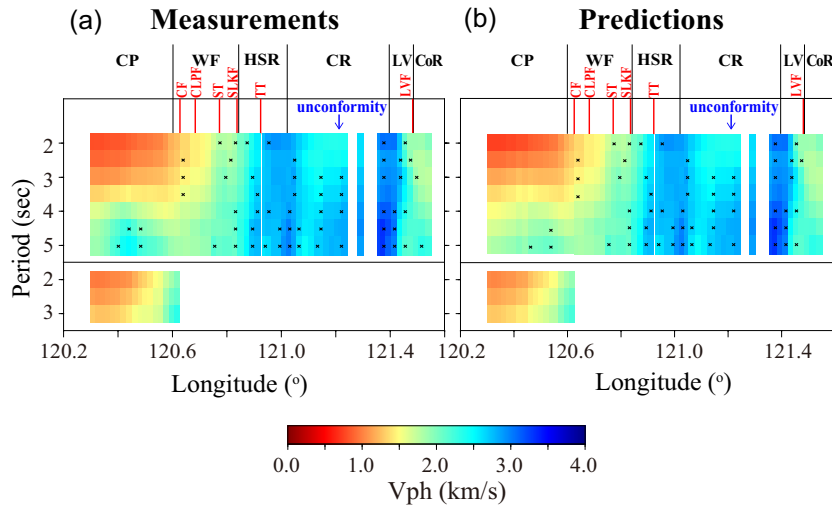


Figure 5. (a) The observed period-dependent phase velocity profiles for both fundamental (top) and higher modes (bottom). The black crosses identify locations with absolute phase velocity second derivative above $280 \text{ s}^{-1} \text{ km}^{-1}$. (b) Same as (a), but for the predicted phase velocity profiles using the inverted 2-D model shown in Fig. 8.

(Fig. 5). We combine the inverted 1-D models from all beam centre locations to construct the final 2-D V_S model.

3 RESULTS

3.1 Phase velocity results

The phase velocity profiles derived from ambient noise cross-correlations and double beamforming (Figs 4 and 5) are generally correlated well with known geological features across central Taiwan. Low phase velocities are observed in the Coastal Plain, particularly at short periods, reflecting the shallow sedimentary deposits. High phase velocities are observed in the Hsueshan Range and the eastern Central Ranges, reflecting the metamorphic core

complexes. Slightly moderate fast velocities are observed in the western Central Ranges correlated with where lower grade metamorphic rocks are exposed to the surface. Both the Western Foothills to the west and the Coastal Range to the east exhibit moderate slow velocities corresponding to the sedimentary structure there. These major velocity structures are typically bounded by locations with high second derivative phase velocity values (Fig. 5) suggesting that the velocity changes are sharp. It is worth noting that elevated second derivative values are also commonly observed within the Western Foothills likely reflecting the discrete velocity jumps across the ramp-up faults. We provide a more detailed discussion of the implication of our result in the later section.

It is worth noting that there are significant elevation changes across the Central Range, with a ~ 10 per cent inclination on each

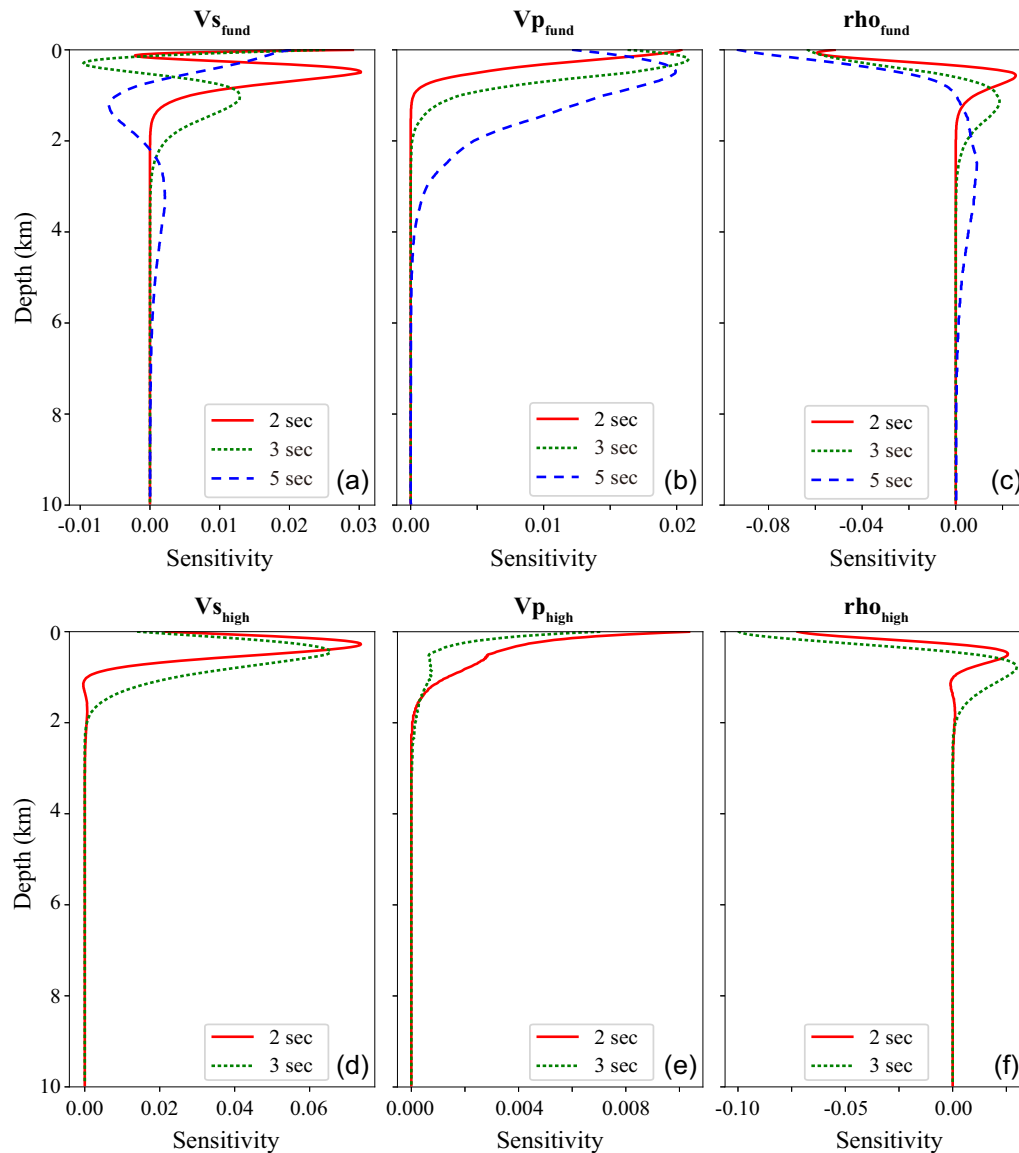


Figure 6. The depth sensitivity kernels of multimode Rayleigh wave phase velocities calculated numerically by perturbing the reference model at the location of station M11 (orange circle in Fig. 1b). (a)–(c) The V_s , V_p and density sensitivity kernels for fundamental-mode Rayleigh waves. (d)–(f) Same as (a)–(c), but for the higher mode.

side (Fig. 4a). In principle, a steep inclination could result in a longer propagation distance for surface waves compared to waves propagating along a flat surface. If the wave is completely bounded to the surface, a 10 per cent inclination would increase the distance by ~ 5 per cent, thereby lowering the observed apparent phase velocity by ~ 5 per cent. This potential bias is significantly smaller than the > 15 per cent phase velocity variations observed across the Central Range at 2 s (Fig. 4b). Moreover, the observed velocity is lowest where elevation approaches its maximum instead of at locations with the highest inclination. These pieces of evidence suggest that the topography effect is not significant when compared to the intrinsic velocity variation related to subsurface structure. At longer periods, the topography variation (2–3 km) is quite small compared to the wavelength (~ 10 km), and hence we expect the potential bias to be even smaller.

To assess the depth sensitivity of our phase velocity measurements, we calculate the 1-D sensitivity kernels numerically by perturbing V_s , V_p and density at different depth (Fig. 6). While it is often assumed that higher-mode Rayleigh waves are more sensitive to deeper structures (e.g. Yoshizawa & Ekström 2010), our sensitivity kernels suggest that it is the fundamental-mode Rayleigh waves that have the deeper sensitivity. Although this is somewhat surprising, it is consistent with the results of Ma *et al.* (2016), which show that the higher-mode Rayleigh wave eigenfunction could be shallower in a sedimentary setting. This unconventional characteristic likely reflects short-period higher-mode energy being nearly completely trapped in shallow slow sediments due to the sharp velocity increase across the basement. This is consistent with the fact that we do not observe any higher-mode signals outside of the Coastal Plain and beyond 3-s period (Fig. 5).

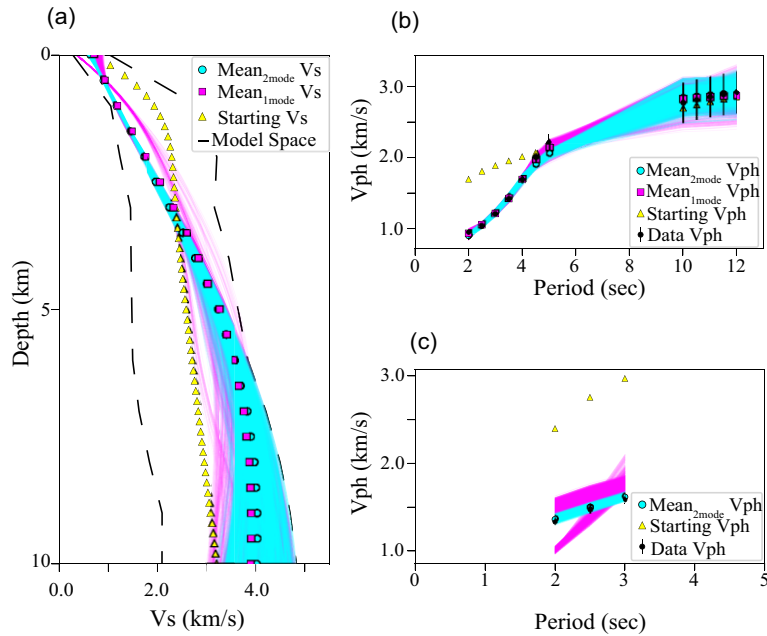


Figure 7. The MCMC inversion. (a) Example 1-D MCMC inversion for beam centre station M11 in Coastal Plain (orange circle in Fig. 1b). Yellow triangles, cyan blue lines and pink lines represent the reference model, the acceptable models for multimode joint inversion and the acceptable models for fundamental-mode-only inversion. The dashed lines indicate the search range, with pink squares representing the mean model for the fundamental-mode-only inversion and cyan circles representing the mean model for the multimode joint inversion. (b) and (c) The observed and predicted fundamental- and higher-mode Rayleigh wave phase velocity dispersion curves from models in (a).

3.2 Multimode MCMC inversion and model comparison

Fig. 7 shows an example of 1-D inversion with/without including higher-mode dispersion measurements in the Coastal Plain. When using only the fundamental-mode dispersion measurements, a bimodal posterior model distribution between 0 and 3 km depth is observed, demonstrating the trade-off between the velocities at shallow and slightly deeper depths. In this case, the predicted higher-mode dispersion curves (Figs 7b and c) are also bimodal between 2- and 3-s periods, suggesting that the higher-mode dispersion can be used to resolve the tradeoff. By including the higher-mode dispersion measurements, the posterior model distribution is now confined between 0–3 km depth where both the predicted higher- and fundamental-mode dispersion curves (Figs 7b and c) agree with the observations. Benefitting from the complementary sensitivity of higher- and fundamental-mode phase velocity measurements (Fig. 6), the velocity contrast between the shallow slow sedimentary structure and the deeper fast basement can be well resolved across the CP, and the depth resolution could be reliable down to at least 5 km depth. Below 5 km, the broad distribution of posterior models reflects the lack of sensitivity in our short-period measurements (Fig. 6).

The inverted 2-D V_s model (Figs 8a and c) illustrates patterns that are majorly consistent with the observed phase velocity profile (Fig. 5a) and known geological features and tectonic settings (i.e. sedimentary deposits, fault systems and mountain belts). The model also overall agrees with the regional reference model derived from body wave tomography (Fig. 8b; Huang *et al.* 2014a). Our new model, however, better delineates the geometry of subsurface fine-scale crustal structures. In Figs 8(a) and (c), we superimpose the structural profile of Yue *et al.* (2005) and the projected background seismicity from 1991 to 2020 onto our model for comparison. Clear correlations can be observed between the inverted velocity structures and known major geological structures including the sharp velocity contrast across the Chinshui Shale beneath the Coastal

Plain, the thickening of the foreland fault-and-thrust belt across the Western Foothills, the overall fast metamorphic complex of the Hsuehshan and Central Ranges and shallow sedimentary structure associated with the Longitudinal Valley and Coastal Range.

4 DISCUSSION

While the 2-D V_s model (Figs 8a and c) preserved some of the sharp transitions observed in the phase velocity profile (Fig. 5a), it is less spatially coherent due to minor instabilities in the 1-D MCMC inversions. Consequently, we are unable to identify some of the small-scale velocity transitions in our V_s model using the second derivative analysis, as we did with the phase velocity profile (Fig. 5a). Instead, we present the velocity contours (Fig. 8a) of the spatially smoothed V_s model, with a grid size of approximately 0.023° to represent the average station distance, highlighting the velocity variation. To only focus our discussion on the most reliable part of the model, we masked out depths where the V_s sensitivity of the 5-s phase velocity is less than 0.001 km^{-1} in our sensitivity kernel analysis (Fig. 6). Generally, the sensitivity kernel tends to move shallower in low-velocity zones due to shorter wavelengths.

4.1 The pro-wedge architecture and pre-orogenic normal faults

Our model further shows the structural details within the doubly vergent accretionary wedge of Taiwan. The western half of the Taiwan island, including Western Foothills, HSR and western part of Central Range, is considered as the pro-wedge, with fold-and-thrust ramping faults propagating above the detachment (Willett & Brandon 2002; Yue *et al.* 2005; Fuller *et al.* 2006). While the slow anomaly from our velocity model (Figs 8a and c) shows an excellent geometrical correlation to the geometry of the foreland

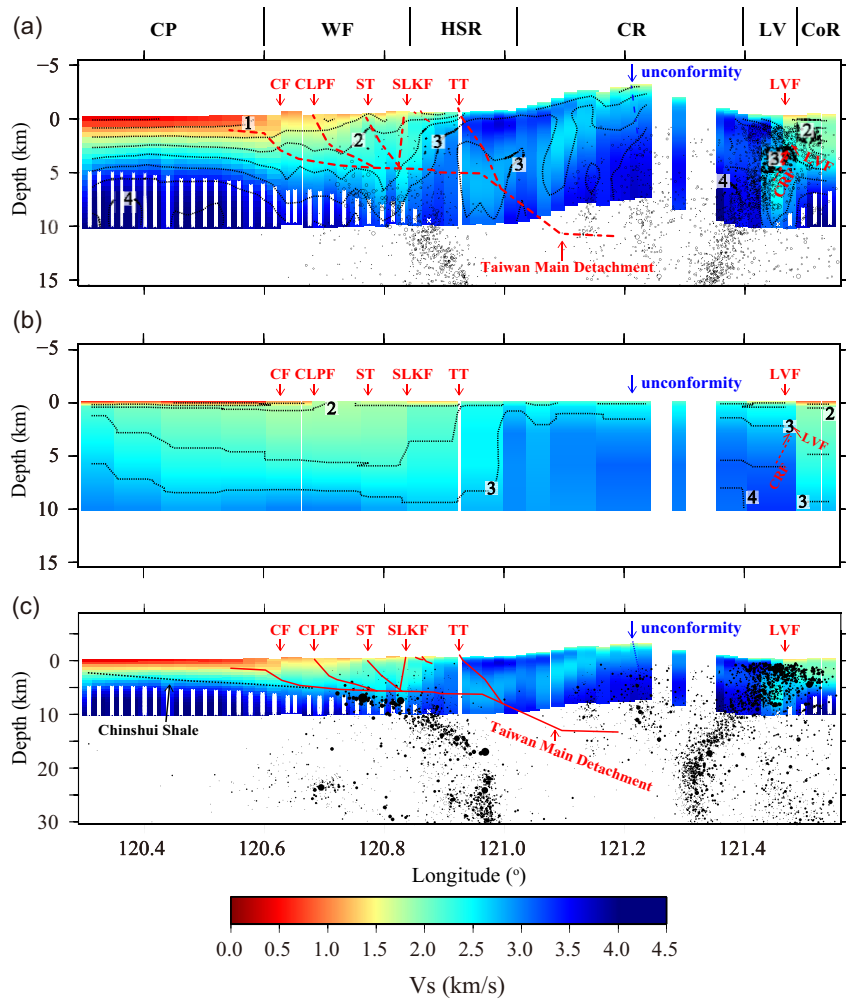


Figure 8. (a) The inverted 2-D V_s model with vertical exaggeration of 2X. The black dotted line marks the 0.5 km s^{-1} velocity contours. The open dots show the background seismicity between 1991 and 2020 (Wu *et al.* 2008). The grey crosses mark areas with low sensitivity in our measurements. The structural/fault profile, modified from Yue *et al.* (2005), in western Taiwan are identified by the red dashed lines. (b) Same as (a), but for the referenced model of Huang *et al.* (2014a). (c) Same as (a), but without vertical exaggeration. The black dots show the same background seismicity as in (a). The black dashed line represents the Chinsui Shale beneath the Coastal Plain and Chiayang Formation west of the Central Range.

basin extracted from Lin & Watts (2002) and fold-and-thrust ramping fault systems within Western Foothill from Yue *et al.* (2005), it also provides more details for understanding the geometry of these structures. We consider V_s 3.0 km s^{-1} (e.g. $\approx V_p$ 5.2 km s^{-1}) as a reference velocity separating crystalline from clastic sedimentary rocks (Brown *et al.* 2022). Background seismicity is mainly observed beneath the V_s 3.0 km s^{-1} contour line, while the pro-wedge's fold-and-thrust system is primarily developed above this V_s 3.0 km s^{-1} velocity contour. This correlation reflects the geometry of Taiwan Main Detachment and the thin-skinned thrust model in western Taiwan.

The shallow velocity in the top 3 km in the pro-wedge generally increases eastward, where apparent velocity increases can be observed across the Changhua Fault (CF), Shuangtung Thrust (ST) and the Shuilikeng Fault (SLKF). Layered unconsolidated sediments with velocities slower than 1.0 km s^{-1} (Fig. 8a) are only observed near the surface west of the CF. This suggests that the CF and its hangingwall anticline served as the deformation front in the pro-wedge, where the foreland basin sediment has been uplifted and eroded (Yue *et al.* 2005). A similar shallow velocity increase can be found across the ST, where velocity in the top 2 km shows

a sharp eastward increase. Note that the velocity change across the ST is much sharper than the change across the CF, suggesting the geometry of the ST is likely steeper than the CF.

In contrast to the shallow velocity increases, step-like eastward velocity drops are observed below $\sim 4 \text{ km}$ depth beneath the CF, ST and Chelungpu Fault (CLPF). These eastward velocity drops have yet to be noticed in the structural profile at this latitude but roughly coincide with where the CF, CLPF and ST are expected to ramp up from the basal detachment. Care must be taken when interpreting these deeper features, as some might reflect trade-off between shallow and deeper structures in the 1-D inversions. At 5-s period, an eastward phase velocity drop can be observed beneath CF in the phase velocity profile (Fig. 5) indicating that at least V_s drop there is a robust feature. We suggest that the divergence of shallow and deep velocity variation hints pre-existing east-dipping normal faults, which were reactivated as reverse faults during the orogeny (Brown *et al.* 2012). Based on the industrial seismic reflection data, Yang *et al.* (2016) suggest similar pre-orogenic normal faults exist underneath the Coastal Plain. Simoes *et al.* (2007) also suggest a high-angle hinge fault exists below the northern part of CF and its anticline, showing similar geometry as we see in our velocity model

across the southern part of the anticline. Our finding, along with other lines of evidence from previous analyses, suggests that the pre-existing normal faults could play a significant role in controlling the structural location and geometry of Taiwan's pro-wedge.

Further east, a sharp velocity increase is observed from the surface down to ~ 10 km across the surface-mapped SLKF, which is a tectonostratigraphic feature separating the sedimentary Western Foothills and metamorphosed HSR. The trend of velocity increase across the SLKF, however, is different from the east-dipping trend across the other faults in the frontal part of the pro-wedge, suggesting the SLKF might be west dipping in contrast to those aforementioned structures. Even though previous studies agreed that the SLKF is the primary feature that separates the synorogenic foreland basin from the metamorphosed zone, the kinematics and detailed structure of the SLKF are still debated and have been explained in various interpretations. For instance, Yue *et al.* (2005) described the SLKF as a pre-existing west-dipping extensional fault; Brown *et al.* (2012) exerted it as a steeply east-dipping transpressional fault that penetrates well into the middle crust; Camanni *et al.* (2014) suggest it as an east-dipping rifted-related fault. From our model, we found that the geometry of the SLKF is consistent with the model proposed by Yue *et al.* (2005) that the SLKF is a high-angle west-dipping fault and could provide structural evidence of pre-rifting tectonic evolution in Taiwan.

4.2 The retro-wedge architecture

On the eastern side of Taiwan, the eastern part of the Central Range and the Longitudinal Valley are categorized as the retro-wedge of the Taiwan orogen, where the reverse CRF acts as the back thrust structure of the wedge (e.g. Chuang *et al.* 2014). On the easternmost part of the 2-D model, we observe a distinct velocity contrast between the Central Range and the Coastal Range, where the high-velocity Central Range is bounded by a steeply west-dipping boundary beneath the range. This velocity contrast matches well with the location of the Longitudinal Valley Suture, which consists of the active high-angle west-dipping CRF and the east-dipping LVF (Shyu *et al.* 2005, 2006). The background seismicity shows a west-dipping cluster and an east-dipping cluster, corresponding to the velocity contrast and delineating the CRF to the west and the LVF to the east. We observed a junction formed between the LVF and CRF approximately at 3 km depth along our velocity profile. This observation is consistent with the interpretation that the CRF is buried beneath the LVF (Shyu *et al.* 2005, 2006; Chuang *et al.* 2014; Lee *et al.* 2014) and subsequently truncates the LVF in the northern Longitudinal Valley (Huang & Wang 2022). The truncation of CRF–LVF plays a crucial part in controlling the coseismic fault propagation for earthquakes generated by the LVF. Also, the velocity contours beneath the surface location of the LVF (Shyu *et al.* 2020) reveal a steep east-dipping velocity contrast, correlating with the imbricate thrusting geometry mentioned in Hsieh *et al.* (2020). Combining the previous geological and seismological observations (Shyu *et al.* 2006; Wu *et al.* 2006; Chuang *et al.* 2014; Huang & Wang 2022) with our inferred geometry of the CRF provides additional structural details between the retro-wedge and Longitudinal Valley suture.

4.3 Fault-and-fold structures within the Central Range

We observe a high-angle east-dipping velocity contrast across the Tili Thrust (TT) within the metamorphic HSR area. The TT is a major structural boundary at the western margin of the metamorphic Central Range (Fig. 8c). Previous studies suggested that the

TT is a steeply dipping fault, where the velocity boundary can be interpreted as a hangingwall ramp against a footwall ramp (Yue *et al.* 2005; Brown *et al.* 2012). Our velocity model also suggests that the TT is a crustal-scale geological boundary that extends to at least 10 km below the surface, with its geometry matching the interpreted structure of the balanced structural profile (Yue *et al.* 2005). Interestingly, the crustal-scale TT is not correlated to any background seismicity from Wu *et al.* (2008). Instead, a seismicity cluster with a similar geometry to that of the TT and its deeper ramp appears underneath the SLKF, very close to the eastward velocity drop described in the previous section. Although our profile does not extend deep enough to observe the velocity change associated with this group of seismicity, Chuang *et al.* (2013) suggest this east-dipping seismicity may be associated with the newly developed duplex system beneath the orogeny belt. While our data cannot prove this hypothesis, like other velocity changes that occurred along the reverse faults within the fold-and-thrust belt in WF, we observe that the location where the seismicity joins the basal detachment aligns with the velocity change in our model. This suggests that the east-dipping seismicity may be associated with a major pre-existing structure within the orogenic belt.

It is worth noting that we also observe the first-order structural geometry within the slate-dominated Central Range. The comparison with the structural profile from Yue *et al.* (2005) indicates that the two relatively low-velocity zones in the western flank of the Central Range are likely associated with synclinoria, where their cores are composed by the Chiayang formation. Also, at ~ 25 km east of the TT, the bowl-shaped velocity drop could imply an unconformity between the Lushan and Pilushan Formations where Mesozoic and Paleozoic schist and marble formations are exposed on the surface along the eastern flank of the Central Range.

5 CONCLUSIONS

In this study, by applying ambient noise double-beamforming tomography across a dense linear geophone array, we construct a detailed 2-D regional crustal shear wave velocity model across central Taiwan. We extract robust Rayleigh wave signals from multicomponent noise cross-correlations, propose an iterative double-beamforming scheme to measure higher- and fundamental-mode phase velocities across the array, and then apply MCMC inversions to construct the final V_S model. The shallow sensitivity of our measurements unveils detailed upper crustal structures with unprecedented resolution. The new model overall is consistent with prior geological and geophysical studies but provides further constraints on the geometry of sedimentary foreland basin and fault systems in central Taiwan. Moreover, the new model provides a clear view of the doubly vergent wedge architecture of Taiwan. For the pro-wedge to the west, the V_S structure reveals detailed geometry of the fold-and-thrust belt and the pre-existing normal faults that may have been reactivated as reverse faults during the orogeny. For the retro-wedge to the east, the CRF is identified as a west-dipping slow anomaly, which is truncated by the east-dipping LVF at ~ 3 km depth. These new findings, combined with previous geological and geophysical observations, illuminate the orogenic processes in Taiwan and provide insight into regional earthquake hazards.

ACKNOWLEDGMENTS

This work was supported by the National Science Foundation of the US (grant EAR-1753362) and the National Science and Technology Council of Taiwan (grant NSTC111-2116-M-001-032). We thank the TAIGER working group for collecting the data, and John Suppe

and Yu-Huan Hsieh for valuable discussion about Taiwan's tectonic and geological structures. We also thank editor Gabi Laske and two anonymous reviewers for their helpful comments.

DATA AVAILABILITY

TAIGER data are accessible on the International Federation of Digital Seismograph Networks (https://doi.org/10.7914/SN/2F_2009). The code to perform double beamforming is available on GitHub (<https://github.com/andrewntu/Double-Beamforming.git>).

REFERENCES

- Bensen, G.D., Ritzwoller, M.H., Barmin, M.P., Levshin, A.L., Lin, F., Moschetti, M.P., Shapiro, N.M. & Yang, Y., 2007. Processing seismic ambient noise data to obtain reliable broad-band surface wave dispersion measurements, *Geophys. J. Int.*, **169**(3), 1239–1260.
- Biq, C.C., 1965. The eastern Taiwan rift, *Petrol. Geol. Taiwan*, **4**, 93–106.
- Brocher, T.M., 2005. Empirical relations between elastic wavespeeds and density in the Earth's crust, *Bull. seism. Soc. Am.*, **95**(6), 2081–2092.
- Brown, D., Alvarez-Marrón, J., Camanni, G., Biete, C., Kuo-Chen, H. & Wu, Y.M., 2022. Structure of the south-central Taiwan fold-and-thrust belt: testing the viability of the model, *Earth Sci. Rev.*, **231**, 104094, doi:10.1016/j.earscirev.2022.104094.
- Brown, D., Alvarez-Marrón, J., Schimmel, M., Wu, Y.M. & Camanni, G., 2012. The structure and kinematics of the central Taiwan mountain belt derived from geological and seismicity data, *Tectonics*, **31**(5), doi:10.1029/2012TC003156.
- Camanni, G., Brown, D., Alvarez-Marrón, J., Wu, Y.M. & Chen, H.A., 2014. The Shuilikeng fault in the central Taiwan mountain belt, *J. geol. Soc.*, **171**(1), 117–130.
- Carena, S., Suppe, J. & Kao, H., 2002. Active detachment of Taiwan illuminated by small earthquakes and its control of first-order topography, *Geology*, **30**(10), 935–938.
- Chang, C.H., Wu, Y.M., Shin, T.C. & Wang, C.Y., 2000. Relocation of the 1999 Chi-Chi earthquake in Taiwan, *Terr. Atmos. Ocean. Sci.*, **11**(3), 581–590.
- Chen, C.T., Lo, C.H., Wang, P.L. & Lin, L.H., 2022. Extensional mountain building along convergent plate boundary: insights from the active Taiwan mountain belt, *Geology*, **50**(11), 1245–1249.
- Chen, W.S. et al. 2001a. 1999 Chi-Chi earthquake: a case study on the role of thrust-ramp structures for generating earthquakes, *Bull. seism. Soc. Am.*, **91**(5), 986–994.
- Chen, Y.G., Chen, W.S., Lee, J.C., Lee, Y.H., Lee, C.T., Chang, H.C. & Lo, C.H., 2001b. Surface rupture of 1999 Chi-Chi earthquake yields insights on active tectonics of central Taiwan, *Bull. seism. Soc. Am.*, **91**(5), 977–985.
- Ching, K.E., Rau, R.J., Johnson, K.M., Lee, J.C. & Hu, J.C., 2011. Present-day kinematics of active mountain building in Taiwan from GPS observations during 1995–2005, *J. geophys. Res.: Solid Earth*, **116**(B9), doi:10.1029/2010JB008058.
- Chuang, R.Y., Johnson, K.M., Kuo, Y.T., Wu, Y.M., Chang, C.H. & Kuo, L.C., 2014. Active back thrust in the eastern Taiwan suture revealed by the 2013 Ruisuei earthquake: evidence for a doubly vergent orogenic wedge?, *Geophys. Res. Lett.*, **41**(10), 3464–3470.
- Chuang, R.Y., Johnson, K.M., Wu, Y.M., Ching, K.E. & Kuo, L.C., 2013. A midcrustal ramp-fault structure beneath the Taiwan tectonic wedge illuminated by the 2013 Nantou earthquake series, *Geophys. Res. Lett.*, **40**(19), 5080–5084.
- Fuller, C.W., Willett, S.D., Fisher, D. & Lu, C.Y., 2006. A thermomechanical wedge model of Taiwan constrained by fission-track thermochronometry, *Tectonophysics*, **425**(1–4), 1–24.
- Gkogkas, K., Lin, F.C., Allam, A.A. & Wang, Y., 2021. Shallow damage zone structure of the Wasatch fault in Salt Lake City from ambient-noise double beamforming with a temporary linear array, *Seismol. Soc. Am.*, **92**(4), 2453–2463.
- Herrmann, R.B., 2013. Computer programs in seismology: an evolving tool for instruction and research, *Seismol. Res. Lett.*, **84**(6), 1081–1088.
- Hsieh, Y.H., Liu, C.S., Suppe, J., Byrne, T.B. & Lallemand, S., 2020. The chimei submarine canyon and fan: a record of Taiwan arc-continent collision on the rapidly deforming overriding plate, *Tectonics*, **39**(11), e2020TC006148, doi:10.1029/2020TC006148.
- Hsu, Y.J., Segall, P., Yu, S.B., Kuo, L.C. & Williams, C.A., 2007. Temporal and spatial variations of post-seismic deformation following the 1999 Chi-Chi, Taiwan earthquake, *Geophys. J. Int.*, **169**(2), 367–379.
- Huang, H.H. & Wang, Y., 2022. Seismogenic structure beneath the northern Longitudinal Valley revealed by the 2018–2021 Hualien earthquake sequences and 3-D velocity model, *Terr. Atmos. Ocean. Sci.*, **33**(1), 17, doi:10.1007/s44195-022-00017-z.
- Huang, H.H., Wu, Y.M., Song, X., Chang, C.H., Kuo-Chen, H. & Lee, S.J., 2014b. Investigating the lithospheric velocity structures beneath the Taiwan region by nonlinear joint inversion of local and teleseismic P wave data: slab continuity and deflection, *Geophys. Res. Lett.*, **41**(18), 6350–6357.
- Huang, H.H., Wu, Y.M., Song, X., Chang, C.H., Lee, S.J., Chang, T.M. & Hsieh, H.H., 2014a. Joint vp and vs tomography of Taiwan: implications for subduction-collision orogeny, *Earth planet. Sci. Lett.*, **392**, 177–191.
- Huang, T.Y., Gung, Y., Kuo, B.Y., Chiao, L.Y. & Chen, Y.N., 2015. Layered deformation in the Taiwan orogen, *Science*, **349**(6249), 720–723.
- Hung, J.H., Ma, K.F., Wang, C.Y., Ito, H., Lin, W. & Yeh, E.C., 2009. Subsurface structure, physical properties, fault-zone characteristics and stress state in scientific drill holes of Taiwan Chelungpu Fault Drilling Project, *Tectonophysics*, **466**(3–4), 307–321.
- Jia, Z. & Clayton, R.W., 2021. Determination of near surface shear-wave velocities in the central Los Angeles basin with dense arrays, *J. geophys. Res.: Solid Earth*, **126**(5), e2020JB021369, doi:10.1029/2020JB021369.
- Jiang, C. & Denolle, M.A., 2022. Pronounced seismic anisotropy in Kanto sedimentary basin: a case study of using dense arrays, ambient noise seismology, and multi-modal surface-wave imaging, *J. geophys. Res.: Solid Earth*, **127**(8), e2022JB024613, doi:10.1029/2022JB024613.
- Johnson, K.M., Hsu, Y.J., Segall, P. & Yu, S.B., 2001. Fault geometry and slip distribution of the 1999 Chi-Chi, Taiwan earthquake imaged from inversion of GPS data, *Geophys. Res. Lett.*, **28**(11), 2285–2288.
- Kao, H. & Chen, W.P., 2000. The Chi-Chi earthquake sequence: active, out-of-sequence thrust faulting in Taiwan, *Science*, **288**(5475), 2346–2349.
- Kuo-Chen, H., Wu, F.T. & Roecker, S.W., 2012. Three-dimensional P velocity structures of the lithosphere beneath Taiwan from the analysis of TAIGER and related seismic data sets, *J. geophys. Res.: Solid Earth*, **117**(B6), doi:10.1029/2011JB009108.
- Kuo, Y.W. et al. 2016. Crustal structures from the Wuyi-Yunkai orogen to the Taiwan orogen: the onshore-offshore wide-angle seismic experiments of the TAIGER and ATSEE projects, *Tectonophysics*, **692**, 164–180.
- Kuo-Chen, H., Wu, Y.M., Chen, Y.G. & Chen, R.Y., 2007. 2003 Mw 6.8 Chengkung earthquake and its related seismogenic structures, *J. Asian Earth Sci.*, **31**(3), 332–339.
- Lai, S.H. & Chern, C.C., 2002. Structural mapping of the 1999 Chi-Chi earthquake fault, Taiwan by seismic reflection methods, doi:10.3319/TAO.2002.13.3.211(CCE).
- Lee, J.C., Chu, H.T., Angelier, J., Chan, Y.C., Hu, J.C., Lu, C.Y. & Rau, R.J., 2002. Geometry and structure of northern surface ruptures of the 1999 Mw= 7.6 Chi-Chi Taiwan earthquake: influence from inherited fold belt structures, *J. Struct. Geol.*, **24**(1), 173–192.
- Lee, S.J., Huang, H.H., Shyu, J.B.H., Yeh, T.Y. & Lin, T.C., 2014. Numerical earthquake model of the 31 October 2013 Ruisui, Taiwan, earthquake: source rupture process and seismic wave propagation, *J. Asian Earth Sci.*, **96**, 374–385.
- Lee, S.J., Liu, T.Y. & Lin, T.C., 2023. The role of the west-dipping collision boundary fault in the Taiwan 2022 Chihshang earthquake sequence, *Sci. Rep.*, **13**(1), 3552. doi:10.1038/s41598-023-30361-0.
- Lin, A.T. & Watts, A.B., 2002. Origin of the West Taiwan basin by orogenic loading and flexure of a rifted continental margin, *J. geophys. Res.: Solid Earth*, **107**(B9), ETG–2. doi:10.1029/2001JB000669.
- Lin, C.D.-J., Wu, Y.-M., Tung, H. & Huang, H.-H. (2024). Coseismic deformation and interaction of the 2022 ML 6.6 Guanshan and ML 6.8

- Chihshang earthquakes in southeastern Taiwan revealed by strong motion data, *Seismol. Res. Lett.* doi:10.1785/0220240130.
- Lin, F.C., Li, D., Clayton, R.W. & Hollis, D., 2013. High-resolution 3D shallow crustal structure in Long Beach, California: application of ambient noise tomography on a dense seismic array, *Geophysics*, **78**(4), Q45–Q56.
- Lin, F.C., Moschetti, M.P. & Ritzwoller, M.H., 2008. Surface wave tomography of the western United States from ambient seismic noise: Rayleigh and Love wave phase velocity maps, *Geophys. J. Int.*, **173**(1), 281–298.
- Lin, F.C., Tsai, V.C. & Schmandt, B., 2014. 3-D crustal structure of the western United States: application of Rayleigh-wave ellipticity extracted from noise cross-correlations, *Geophys. J. Int.*, **198**(2), 656–670.
- Liu, C.N., Lin, F.C., Huang, H.H., Wang, Y., Berg, E.M. & Lin, C.H., 2021. High-resolution 3-D shear wave velocity model of northern Taiwan via bayesian joint inversion of Rayleigh wave ellipticity and phase velocity with Formosa array, *J. geophys. Res.: Solid Earth*, **126**(5), e2020JB021610, doi:10.1029/2020JB021610.
- Ma, Y., Clayton, R.W. & Li, D., 2016. Higher-mode ambient-noise Rayleigh waves in sedimentary basins, *Geophys. J. Int.*, **206**(3), 1634–1644.
- Okaya, D., Wu, F., Wang, C.Y., Yen, H.Y., Huang, B.S., Brown, L. & Liang, W.T., 2009. Joint passive/controlled source seismic experiment across Taiwan, *EOS, Trans. Am. geophys. Un.*, **90**(34), 289–290.
- Rabade, S., Lin, F.C., Tape, C., Ward, K.M., Waldien, T. & Allam, A., 2023. The crustal magmatic structure beneath the Denali Volcanic Gap imaged by a dense linear seismic array, *J. geophys. Res.: Solid Earth*, **128**(12), e2023JB027152, doi:10.1029/2023JB027152.
- Savage, M.K., Lin, F.C. & Townend, J., 2013. Ambient noise cross-correlation observations of fundamental and higher-mode Rayleigh wave propagation governed by basement resonance, *Geophys. Res. Lett.*, **40**(14), 3556–3561.
- Shapiro, N.M., Campillo, M., Stehly, L. & Ritzwoller, M.H., 2005. High-resolution surface-wave tomography from ambient seismic noise, *Science*, **307**(5715), 1615–1618.
- Shen, W., Ritzwoller, M.H., Schulte-Pelkum, V. & Lin, F.C., 2013. Joint inversion of surface wave dispersion and receiver functions: a Bayesian Monte-Carlo approach, *Geophys. J. Int.*, **192**(2), 807–836.
- Shin, T.C. & Teng, T.L., 2001. An overview of the 1999 Chi-Chi, Taiwan, earthquake, *Bull. seism. Soc. Am.*, **91**(5), 895–913.
- Shyu, J.B.H., Sieh, K. & Chen, Y.G., 2005. Tandem suturing and disarticulation of the Taiwan orogen revealed by its neotectonic elements, *Earth planet. Sci. Lett.*, **233**(1–2), 167–177.
- Shyu, J.B.H., Sieh, K., Avouac, J.P., Chen, W.S. & Chen, Y.G., 2006. Millennial slip rate of the Longitudinal Valley fault from river terraces: implications for convergence across the active suture of eastern Taiwan, *J. geophys. Res.: Solid Earth*, **111**(B8), doi:10.1029/2005JB003971.
- Shyu, J.B.H., Yin, Y.H., Chen, C.H., Chuang, Y.R. & Liu, S.C., 2020. Updates to the on-land seismogenic structure source database by the Taiwan Earthquake Model (TEM) project for seismic hazard analysis of Taiwan, *Terr. Atmos. Ocean. Sci.*, **31**(4), 469, doi:10.3319/TAO.2020.06.08.01.
- Simoes, M., Avouac, J.P., Chen, Y.G., Singhvi, A.K., Wang, C.Y., Jaiswal, M., Chan, Y.C. & Bernard, S., 2007. Kinematic analysis of the Pakuashan fault tip fold, west central Taiwan: shortening rate and age of folding inception, *J. geophys. Res.: Solid Earth*, **112**(B3), doi:10.1029/2005JB004198.
- Suppe, J., 1981. Mechanics of mountain building and metamorphism in Taiwan, *Mem. Geol. Soc. China*, **4**(6), 67–89.
- Suppe, J., 1984. Kinematics of arc-continent collision, flipping of subduction, and back-arc spreading near Taiwan. *Geological Society of China Memoir*, **6**, 131–146.
- Tang, C.H. *et al.* 2023. Nearby fault interaction within the double-vergence suture in eastern Taiwan during the 2022 Chihshang earthquake sequence, *Commun. Earth Environ.*, **4**(1), 333, doi:10.1038/s43247-023-00994-0.
- Tanimoto, T. & Rivera, L., 2005. Prograde Rayleigh wave particle motion, *Geophys. J. Int.*, **162**(2), 399–405.
- Teng, L.S., 1990. Geotectonic evolution of late cenozoic arc-continent collision in Taiwan, *Tectonophysics*, **183**(1–4), 57–76.
- Tokimatsu, K., Tamura, S. & Kojima, H., 1992. Effects of multiple modes on Rayleigh wave dispersion characteristics, *J. geotech. Eng.*, **118**(10), 1529–1543.
- Tsai, Y.B., 1986. Seismotectonics of Taiwan, *Tectonophysics*, **125**(1–3), 17–37.
- Van Avendonk, H.J. *et al.* 2016. A lithospheric profile across northern Taiwan: from arc-continent collision to extension, *Geophys. J. Int.*, **204**(1), 331–346.
- Van Avendonk, H.J.A. *et al.* 2014. Deep crustal structure of an arc-continent collision: constraints from seismic traveltimes in central Taiwan and the Philippine Sea, *J. geophys. Res.: Solid Earth*, **119**(11), 8397–8416.
- Wang, C.Y., Tanaka, H., Chow, J., Chen, C.C. & Hong, J.H., 2002. Shallow reflection seismics aiding geological drilling into the Chelungpu fault after the 1999 Chi-Chi earthquake, Taiwan, *Terr. Atmos. Ocean. Sci.*, **13**(2), 153–170.
- Wang, Y., Allam, A. & Lin, F.-C., 2019a. Imaging the Fault damage zone of the San Jacinto Fault near Anza with ambient noise tomography using a dense nodal array, *Geophys. Res. Lett.*, **46**, 12938–12948.
- Wang, Y., Lin, F.C. & Ward, K.M., 2019b. Ambient noise tomography across the Cascadia subduction zone using dense linear seismic arrays and double beamforming, *Geophys. J. Int.*, **217**(3), 1668–1680.
- Willett, S., Beaumont, C. & Fullsack, P., 1993. Mechanical model for the tectonics of doubly vergent compressional orogens, *Geology*, **21**(4), 371–374.
- Willett, S.D. & Brandon, M.T., 2002. On steady states in mountain belts, *Geology*, **30**(2), 175–178.
- Wu, H.Y., Ma, K.F., Zoback, M., Boness, N., Ito, H., Hung, J.H. & Hickman, S., 2007. Stress orientations of Taiwan Chelungpu-Fault Drilling Project (TCDFP) hole-A as observed from geophysical logs, *Geophys. Res. Lett.*, **34**(1), doi:10.1029/2006GL028050.
- Wu, Y.M. *et al.* 2006. Coseismic versus interseismic ground deformations, fault rupture inversion and segmentation revealed by 2003 Mw 6.8 Chengkung earthquake in eastern Taiwan, *Geophys. Res. Lett.*, **33**(2), doi:10.1029/2005GL024711.
- Wu, Y.M., Chang, C.H., Zhao, L., Teng, T.L. & Nakamura, M., 2008. A comprehensive relocation of earthquakes in Taiwan from 1991 to 2005, *Bull. seism. Soc. Am.*, **98**(3), 1471–1481.
- Yang, K.M., Rau, R.J., Chang, H.Y., Hsieh, C.Y., Ting, H.H., Huang, S.T., Wu, J.C. & Tang, Y.J., 2016. The role of basement-involved normal faults in the recent tectonics of western Taiwan, *Geol. Mag.*, **153**(5–6), 1166–1191.
- Yao, H., van Der Hilst, R.D. & De Hoop, M.V., 2006. Surface-wave array tomography in SE Tibet from ambient seismic noise and two-station analysis—I. Phase velocity maps, *Geophys. J. Int.*, **166**(2), 732–744.
- Yen, H.Y., Yeh, Y.H. & Wu, F.T., 1998. Two-dimensional crustal structures of Taiwan from gravity data, *Tectonics*, **17**(1), 104–111.
- Yoshizawa, K. & Ekström, G., 2010. Automated multimode phase speed measurements for high-resolution regional-scale tomography: application to North America, *Geophys. J. Int.*, **183**(3), 1538–1558.
- Yu, S.B. & Chen, H.Y., 1994. Global positioning system measurements of crustal deformation in the Taiwan arc-continent collision zone, *Terr. Atmos. Ocean. Sci.*, **5**(4), 477–498.
- Yue, L.F., Suppe, J. & Hung, J.H., 2005. Structural geology of a classic thrust belt earthquake: the 1999 Chi-Chi earthquake Taiwan (Mw= 7.6), *J. Struct. Geol.*, **27**(11), 2058–2083.